

Effects of double parabolic profiles with groove textures on the hydrodynamic lubrication performance of journal bearing under steady operating conditions

Chongpei Liu, Wanyou Li, Xiqun Lu*, and Bin Zhao

College of Power and Energy Engineering, Harbin Engineering University, Harbin, PR China

Received: 22 April 2019 / Accepted: 8 July 2019

Abstract. The textures on the bushing surface have important effects on the performance of journal bearing. In this study, the effects of double parabolic profiles with groove textures on the hydrodynamic lubrication performance of journal bearing under steady operating conditions are investigated theoretically. The journal misalignment, asperity contact and thermal effects are considered, while the profile modifications due to running-in are neglected. The Winkler/Column model is used to calculate the elastic deformation of bushing surface and the adiabatic flow hypothesis is adopted to obtain the effective temperature of lubricating oil. The numerical solution is established by using finite difference and overrelaxation iterative methods, and the rupture zone of oil film is determined by Reynolds boundary conditions. The numerical results reveal that the double parabolic profiles with groove textures with proper location and geometric sizes can increase load carrying capacity and reduce friction loss under steady operating conditions, which effectively overcome the drawbacks of double parabolic profiles. This novel bushing profile may help to reduce the bushing edge wear and enhance the lubrication performance of journal bearing.

Keywords: Journal bearing / double parabolic profiles / groove textures / load carrying capacity / friction loss

1 Introduction

Journal bearing is one of the most critical friction pairs in diesel engine, whose lubrication performance directly affects its reliability and durability. As the journal misalignment, deformation, machining and installation errors are unavoidable in practice, the bushing edge wear is found, as illustrated in [Figure 1](#).

Earlier studies [1–5] had shown that the properly selected bushing profiles can enhance the lubrication performance and reduce the asperity contact. Recently, Liu et al. [6] investigated the effects of bushing profiles on the elastohydrodynamic lubrication performance of the journal bearing under steady operating conditions, which revealed that the double parabolic profiles can reduce the bushing edge wear effectively. However, this profile also reduces the load carrying capacity and increases the hydrodynamic friction loss in some extents. Hence, some techniques should be applied to overcome its drawbacks.

For mechanical components, surface texturing has become a feasible way to improve the contact performance in terms of minimum film thickness, friction, wear and load

carrying capacity [37]. Specially, studies on the effects of surface textures on the performance of journal bearing have attracted wide attentions to scholars. Ji et al. [7] developed a deterministic model for micro-dimple textured rough surfaces to predict hydrodynamic pressure distribution, which showed that the load carrying capacity can be increased significantly with optimum micro-dimple depth and density. Manser et al. [8] presented a detailed investigation related to the effects of three textures, square, cylindrical, and triangular textures, with considering the journal misalignment. Their results indicated that square textures appeared to be superior to other cases to improve the bearing performance. Shinde and Pawar [9] analyzed the effects of partial grooving on the performance of journal bearing by COMSOL software, which showed that the maximum decrease in frictional loss is observed for partially grooving along 90–360° region. Based on the genetic algorithm, Zhang et al. [10,11] developed a numerical model to optimize the texture areas on bushing surface, and the results showed that the semi-elliptical area is optimized than other arrangements. Meng et al. [12,13] investigated the effects of compound textures on the acoustic and lubrication performances of journal bearing, which showed that the compound textures are superior to the simple textures on the performance improvement.

* e-mail: luxiqun@hrbeu.edu.cn

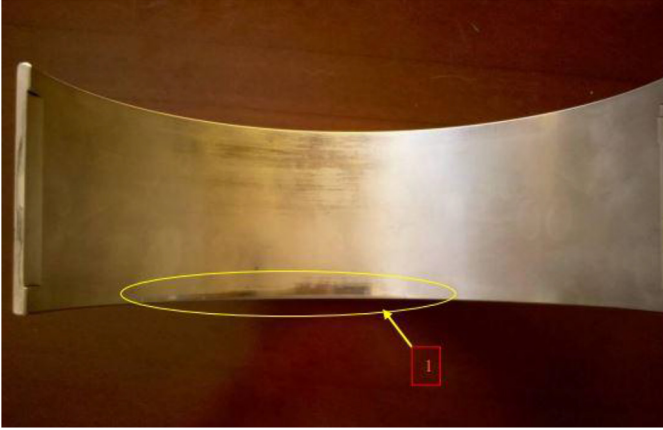


Fig. 1. Edge wear of bearing bushing.

Yamada et al. [14,15] investigated the dynamic and static characteristics of journal bearings with square dimples theoretically and experimentally, which indicated that the square dimples can reduce the absolute value of cross-coupled stiffness coefficients, while other dynamic coefficients show insignificant change, and the dimples can also reduce the load carrying capacity. Gu et al. [16] presented a mixed lubrication model to analyze the performance of the journal bearing with groove textures operating from mixed to hydrodynamic lubrication regime, and the influences of fluid piezoviscosity and non-Newtonian behaviors are also taken into consideration. Morris et al. [17] investigated the effects of textured surface in a partial pad journal bearing by experiments. Their results showed the effective load bearing region is extended due to micro-hydrodynamic effect, which can improve the load carrying capacity. Zhang et al. [18] analyzed the hydrodynamic effects of textures on the journal bearing, and their study shows that the textures with appropriate configuration can increase its load bearing capacity and reduce its cavitation area. Wang et al. [19] investigated the thermohydrodynamic performance of a partial texturing bearing based on a 3D thermohydrodynamic model, and the results showed the partial textures can positively affect the bearing performance under heavy load and high-speed operations. Matele and Pandey [20] developed a numerical model to investigate the effects of texture locations on the bushing surface, which showed that compared with the plain journal bearing, the partial textured bearing with proper location is found to be more stable. Yu et al. [21] investigated the effects of surface texture and flexibility on the performance of journal bearing theoretically. Their results showed that when the textures are located at the rising phase of the pressure field, higher texture density can increase load carrying capacity, while the textures are located at the falling phase of the pressure field, it is harmful to the load carrying capacity. Based on the fluid-structure interaction (FSI) method, Lin et al. [22] investigated the effects of surface textures on the performance of the journal bearing working under transient conditions, and their results indicated that the textures locating at the pressure build-up region will enhance the load carrying capacity, while textures locating at pressure drop region will reduce load

carrying capacity. Shinde and Pawar [23] used a multi-objective optimization method to determine the optimal texture design to increase the load carrying capacity and reduce frictional torque. Tala-Ighil and Fillon [24,25] investigated the texture location effects on the bushing surface of a journal bearing under stationary loads, which indicated that compared with the smooth case, full texturing arrangement poorly affect the bearing performance, while partially texturing arrangements have a positive effect. The texture locations have been proved to be a key influence factor on the bearing performance.

Despite of remarkable progress in research of journal bearings with surface textures, there is few studies has been devoted to apply the textures to enhance the performance of journal bearing with bushing edge wear. Based on the research of Liu et al. [6], this paper theoretically investigates the effects of double parabolic profiles with groove textures on hydrodynamic lubrication performance of journal bearing under steady operating conditions, which aims to overcome the drawbacks of double parabolic profiles mentioned in the second paragraph of introduction. The journal misalignment, asperity contact and thermal effects are considered in this study, and the numerical results reveal that, compared with the double parabolic profiles, the double parabolic profile with groove textures with proper location and geometric parameters can effectively increase the load carrying capacity and reduce the friction loss under steady operating conditions, which is conducive to reduce bushing edge wear and enhance journal bearing performance.

2 Theoretical formulation

2.1 Geometric model

Figure 2 illustrates the three bushing profiles investigated in this study, plain profile, double parabolic profiles and double parabolic profiles with groove textures.

In Figure 2a, B is the width of plain profile, d the thickness of plain profile. In Figure 2b, double parabolic profiles defined by axial width L_y and radial height L_z distribute along the axial direction symmetrically, and the parabolic equation is $\delta_z = (L_z/L_y^2) y^2$. In Figure 2c, a certain number of grooves distribute along the axial direction in specified region, which will be introduced in the following sections. Note the profile modifications due to running-in are not considered here.

2.2 Film thickness

Figure 3 illustrates a misaligned journal bearing with double parabolic profiles and groove textures, whose lubricating oil is supplied through the axial oil feeding groove. For simplicity, only the misalignment in vertical plane yo is considered.

As the hardness of the journal is much higher than that of bearing bushing, only elastic deformation of bushing surface is taken into consideration. Thus, the film thickness h is

$$h = h_g + \delta_e \quad (1)$$

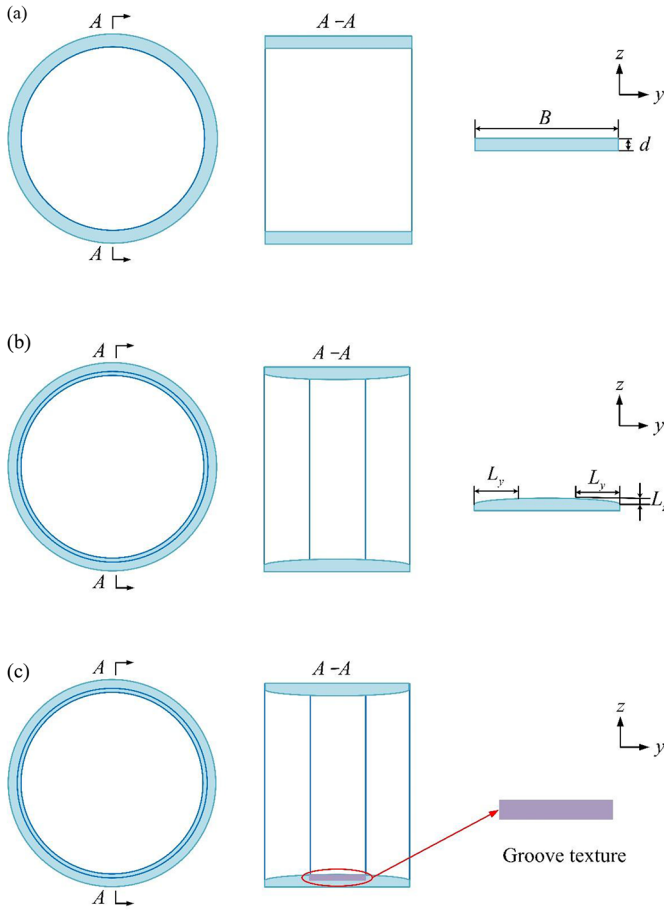


Fig. 2. (a) Plain profile, (b) double parabolic profiles, (c) double parabolic profiles with groove textures.

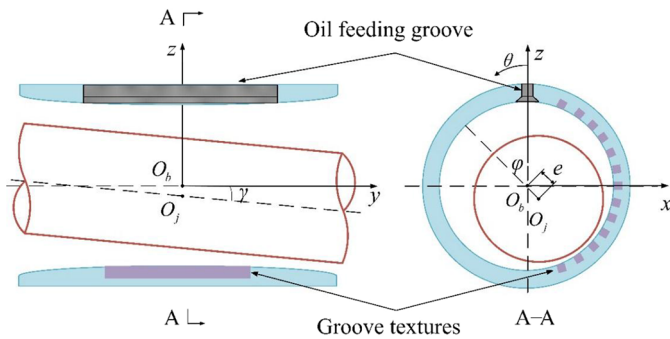


Fig. 3. A misaligned journal bearing with double parabolic profiles and groove textures.

where h_g is the film thickness without elastic deformation, which is given by

$$h_g = c + (e + y \tan \gamma) \cos(\theta - \varphi) + \delta_z + \delta_d \quad (2)$$

where c is the radial clearance, e the eccentricity of the midplane, φ the attitude angle of the midplane, y the axial coordinate, γ the misalignment angle, δ_z the variation clearance caused by the double parabolic profiles, δ_{tex} the

variation clearance caused by the groove textures. Obviously, for the journal bearing with plain profile, $\delta_z = \delta_{tex} = 0$, and for the journal bearing with only double parabolic profiles, $\delta_{tex} = 0$.

In this study, the elastic deformation δ_e is obtained by the Winkler/Column model [26], which provides a simpler way than finite element method [27] to estimate elastic deformation and has been used in some literatures [21,28–30]. The utilized model assumes that the local elastic deformation is only dependent on the local film pressure, as expressed in equation (3)

$$\delta_e = \frac{(1 + \nu)(1 - 2\nu)}{(1 - \nu)} \frac{d}{E} p \quad (3)$$

where ν is the Poisson's ratio of the bushing, E the elastic modulus of the bushing, p the film pressure applied on the bushing surface.

2.3 Reynolds equation

The Reynolds equation based on average flow model is utilized to determine the roughness effects on the lubrication performance of journal bearing [31,32], as expressed in equation (4)

$$\begin{aligned} \frac{\partial}{\partial x} \left(\phi_x \frac{h^3}{12\mu} \cdot \frac{\partial p}{\partial x} \right) + \frac{\partial}{\partial y} \left(\phi_y \frac{h^3}{12\mu} \cdot \frac{\partial p}{\partial y} \right) \\ = \frac{U_1 + U_2}{2} \frac{\partial h_T}{\partial x} + \frac{U_1 - U_2}{2} \sigma \frac{\partial \phi_s}{\partial x} + \frac{\partial h_T}{\partial t} \end{aligned} \quad (4)$$

where μ is the viscosity of lubricating oil, p the film pressure, U_1 and U_2 the velocities of two surfaces, σ the standard deviation of combined roughness, ϕ_x , ϕ_y the pressure flow factors, ϕ_s the shear flow factor, h_T the local film thickness.

For the journal bearing under steady operating conditions, equation (4) can be expressed as followed by the variable transformation $x = R\theta$

$$\begin{aligned} \frac{1}{R^2} \frac{\partial}{\partial \theta} \left(\phi_x \frac{h^3}{\mu} \cdot \frac{\partial p}{\partial \theta} \right) + \frac{\partial}{\partial y} \left(\phi_y \frac{h^3}{\mu} \cdot \frac{\partial p}{\partial y} \right) \\ = 6\omega \frac{\partial h_T}{\partial \theta} + 6\omega\sigma \frac{\partial \phi_s}{\partial \theta} \end{aligned} \quad (5)$$

where ω is angular velocity of journal.

2.4 Asperity contact pressure

The asperity contact model proposed by Greenwood and Tripp [33] is utilized here to estimate interaction effects of asperities, which is widely used in the analysis of rough surfaces contact of the journal bearing. The asperity contact pressure P_{asp} is given by

$$P_{asp} = \frac{16\sqrt{2}\pi}{15} (\eta\beta\sigma)^2 \sqrt{\frac{\sigma}{\beta}} E_c \cdot F_{2.5}(h/\sigma) \quad (6)$$

where η is the number of asperities per unit area, β the mean radius of curvature of the asperities, σ the standard derivation, E_c the composite elastic modulus, $F_{2.5}(h/\sigma)$ the

Gaussian distribution function. Note the surface pattern parameter γ is assumed as 1 here, which means the roughness structures are isotropic.

2.5 Friction loss

It is assumed that when the journal bearing operates in the mixed lubrication regime, the total friction force consists of hydrodynamic friction force arising from the shearing of lubricating oil and asperity contact friction force [34]. Hence, the total friction force f is

$$f = \int_0^B \int_0^{2\pi} \left(\frac{\mu U}{h} (\phi_f + \phi_{fs}) + \phi_{fp} \frac{h}{2R} \frac{\partial p}{\partial \theta} + \mu_{asp} p_{asp} \right) R d\theta dy \quad (7)$$

where $U = \omega R$, ϕ_f , ϕ_{fs} , ϕ_{fp} are the shear stress factors, μ_{asp} boundary friction coefficient. The friction loss P_f can be calculated by

$$P_f = fU. \quad (8)$$

2.6 Leakage flowrate

The leakage flowrate Q_1 from the front-end plane of bearings and the leakage flowrate Q_2 from the rear end plane of bearings are [27]

$$\begin{cases} Q_1 = - \int_0^{2\pi} \phi_y \frac{h^3}{12\mu} \frac{\partial p}{\partial y} \Big|_{y=0} R d\theta \\ Q_2 = - \int_0^{2\pi} \phi_y \frac{h^3}{12\mu} \frac{\partial p}{\partial y} \Big|_{y=B} R d\theta \end{cases} \quad (9)$$

The total leakage flowrate Q is

$$Q = |Q_1| + |Q_2|. \quad (10)$$

2.7 Thermal effects

As well known, the temperature of lubricating oil will increase and its viscosity will decrease exponentially during the operation, so it is more accurate to adopt a variable viscosity model in the calculation. In this study, an effective temperature is obtained based on the adiabatic flow hypothesis of the lubricating oil, as shown below

$$T_e = T_i + k \frac{P_f}{Q \rho c_i} \quad (11)$$

where T_e is the effective temperature of lubricating oil, T_i the inlet oil temperature, P_f the friction loss, Q the total leakage flowrate, ρ the density of lubricating oil, c_i the specific heat of lubricating oil, k the correction factor and $k=0.9$ [35]. This simple fast method avoids the complex computation of thermohydrodynamic lubrication and has been used in the literatures [25,30].

CD40 lubricating oil is used here and its viscosity-temperature equation can be expressed as

$$\ln \left(\frac{1}{a} \ln(1000\mu) \right) = bT_e^2 + cT_e \quad (12)$$

where the unit of μ is Pa. s, and $a = 6.163$, $b = 8.721 \times 10^{-5}$, $c = -0.0455$, respectively. Once the effective temperature is obtained, the effective viscosity can be calculated by the equation (12).

2.8 Load equilibrium

In this study, the external load is applied on journal in the form of pure moment whose direction is parallel to x axis, which only leads to the journal misalignment in vertical plane yoz . The static equilibrium of the journal center can be described as

$$\mathbf{M}_e + \mathbf{M}_t = \mathbf{0} \quad (13)$$

where \mathbf{M}_e is the external moment, \mathbf{M}_t the resultant moment of hydrodynamic moment \mathbf{M}_{oil} and asperity contact moment \mathbf{M}_{asp} , namely $\mathbf{M}_t = \mathbf{M}_{oil} + \mathbf{M}_{asp}$.

The load equilibrium equations along x and z axis are

$$\begin{cases} M_{ex} + M_{tx} = 0 \\ M_{ez} + M_{tz} = 0 \end{cases} \quad (14)$$

where M_{ex} and M_{ez} are the external moment along x and z axis, M_{tx} and M_{tz} the resultant moment along x and z axis, which can be expressed as follows

$$\begin{cases} M_{tx} = M_{oilx} + M_{aspx} \\ M_{tz} = M_{oilz} + M_{aspz} \end{cases} \quad (15)$$

where M_{oilx} and M_{oilz} are the hydrodynamic moment along x and z axis, M_{aspx} and M_{aspz} the asperity contact moment along x and z axis, which can be calculated by

$$\begin{cases} M_{oilx} = + \int_0^B \int_0^{2\pi} ypR \sin \theta d\theta dy \\ M_{oilz} = - \int_0^B \int_0^{2\pi} ypR \cos \theta d\theta dy \end{cases} \quad (16)$$

$$\begin{cases} M_{aspx} = + \int_0^B \int_0^{2\pi} yp_{asp} R \sin \theta d\theta dy \\ M_{aspz} = - \int_0^B \int_0^{2\pi} yp_{asp} R \cos \theta d\theta dy \end{cases} \quad (17)$$

3 Numerical procedure and verification

Apply the finite difference method to discretize the equation (5), then solve the difference equations by overrelaxation iterative method. The Reynolds boundary

conditions are adopted to determine the rupture zone of oil film, while the pressures in the oil feeding groove and both bearing ends are set to zero (ambient pressure) [14,15]. All negative pressures are set to zero during the solution and the discretized film pressure can be calculated by

$$p_{i,j}^{(k_p+1)} = p_{i,j}^{(k_p)} - \omega_s \times \left[p_{i,j}^{(k_p)} - \left(\begin{array}{c} DD_{i,j} - CS_{i,j} \cdot p_{i+1,j}^{(k_p)} - CN_{i,j} \cdot p_{i-1,j}^{(k_p+1)} \\ -CE_{i,j} \cdot p_{i,j+1}^{(k_p)} - CW_{i,j} \cdot p_{i,j-1}^{(k_p+1)} \end{array} \right) / CC_{i,j} \right] \quad (18)$$

where $p_{i,j}^{(k_p+1)}$ is the film pressure for node (i, j) at the (k_p+1) th iteration, $p_{i,j}^{(k_p)}$ the film pressure for node (i, j) at the k_p th iteration, ω_s the overrelaxation factor, here $\omega_s=1.5$. $DD_{i,j}$, $CS_{i,j}$, $CN_{i,j}$, $CE_{i,j}$, $CW_{i,j}$, $CC_{i,j}$ are the difference coefficients during the pressure solution.

The film pressure convergence criteria at the k_p th iteration is given by

$$\frac{\sum_{j=1}^{n_\theta} \sum_{i=1}^{n_y} \left| p_{i,j}^{(k_p+1)} - p_{i,j}^{(k_p)} \right|}{\sum_{j=1}^{n_\theta} \sum_{i=1}^{n_y} p_{i,j}^{(k_p+1)}} \leq \varepsilon_p \quad (19)$$

where ε_p is the allowable precision for the solution of pressure, here $\varepsilon_p = 10^{-5}$. n_θ and n_y are the nodes numbers along the circumferential and axial direction.

Based on the equation (11), the effective temperature convergence criteria at the k_t th iteration is given by

$$\frac{|T_e^{(k_t+1)} - T_e^{(k_t)}|}{T_e^{(k_t+1)}} \leq \varepsilon_t \quad (20)$$

where ε_t is the allowable precision for the solution of the effective temperature, here $\varepsilon_t = 10^{-4}$.

When journal bearing is in the steady operations, it can be assumed that the resultant moment of hydrodynamic and asperity contact moments is approximately equal to the external moment, specifically, the motion of journal can be obtained by correcting the eccentricity ratio ε ($\varepsilon = e/c$), attitude angle φ and misalignment angle γ . The correction strategies can be expressed as follows

$$\varphi = \varphi + \omega_\varphi \arctan \left(\frac{M_{tx}}{M_{tz}} \right) \quad (21)$$

$$\left\{ \begin{array}{l} \varepsilon = \varepsilon - \omega_\varepsilon \left(\frac{M_t}{M_e} - 1 \right) \left(\frac{M_t}{M_e} \geq 1 \right) \\ \varepsilon = \varepsilon + \omega_\varepsilon \left(1 - \frac{M_t}{M_e} \right) \left(\frac{M_t}{M_e} < 1 \right) \end{array} \right. \quad (22)$$

$$\left\{ \begin{array}{l} \gamma = \gamma - \omega_\gamma \left(\frac{M_t}{M_e} - 1 \right) \left(\frac{M_t}{M_e} \geq 1 \right) \\ \gamma = \gamma + \omega_\gamma \left(1 - \frac{M_t}{M_e} \right) \left(\frac{M_t}{M_e} < 1 \right) \end{array} \right. \quad (23)$$

where M_e is the amplitude of \mathbf{M}_e , M_t amplitude of \mathbf{M}_t , ω_φ , ω_ε , ω_γ correction factors of φ , ε , γ . The initial values of φ , ε , γ are $\varphi_0 = \pi$ rad, $\varepsilon_0 = 0.9$, $\gamma_0 = 2 \times 10^{-4}$ rad, and $\omega_\varphi = 0.9$, $\omega_\varepsilon = 1 \times 10^{-2}$, $\omega_\gamma = 1 \times 10^{-5}$, respectively.

As mentioned previously, the external load is a pure moment whose direction is parallel to x axis. So, the equilibrium convergence criteria can be given by

$$\left| \frac{M_{tx}}{M_{tz}} \right| \leq err_{xz} \quad (24)$$

$$\frac{|M_t - M_e|}{M_e} \leq err_M \quad (25)$$

where err_{xz} and err_M are allowable precisions for the equilibrium calculation, here $err_{xz} = 10^{-3}$, $err_M = 10^{-3}$.

The whole computational process is shown in Figure 4. The MATLAB R2015b is used to conduct the numerical solution, and the configurations of computer are: Intel Xeon CPU E5-2690, 2.90GHz, RAM 256G.

Before the analysis of double parabolic profiles with groove textures, it is necessary to validate the calculation model. The calculated film pressures of the journal bearing with plain profile are compared with Ferron's experimental results [36], as illustrated in Figure 5. The comparisons show that the calculated results agree well with the experimental ones, which confirms the validity of this model.

4 Results and discussions

The detailed parameters of the journal bearing investigated in this study are listed in Table 1.

Mesh refinement analysis is conducted based on the journal bearing with plain profile. Various mesh schemes and corresponding minimum film thickness (h_{\min}) are listed in Table 2. It can be seen that h_{\min} is converged when the mesh is 1441×181 . Considering the solving time and accuracy, 1441×181 mesh is adopted.

As mentioned in [6], the journal bearing with double parabolic profiles has a better performance than that with plain profile regarding reducing edge wear. Here one typical case is conducted to illustrate the performance comparisons between plain profile and double parabolic profiles (axial width $L_y = 0.1B$, radial height $L_z = 2\mu m$), then the double parabolic profiles with groove textures are mainly discussed. Parameters used to evaluate the performance are listed in Table 3, and the relative variations of each performance parameter is defined as below

$$\delta_{dpp} X = \frac{X_{dpp} - X_{pp}}{X_{pp}} \times 100\% \quad (26)$$

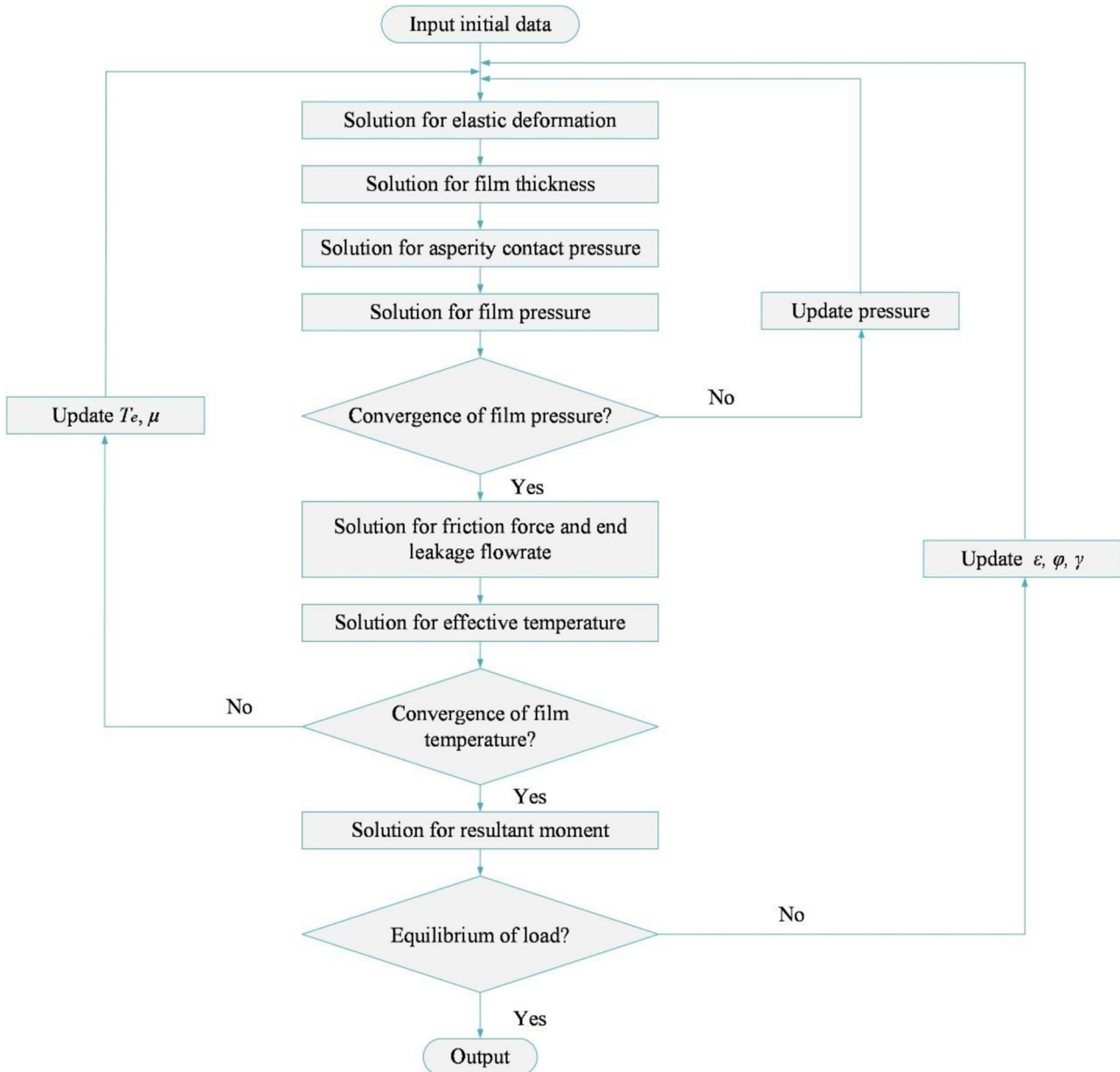


Fig. 4. Flow chart of the computational process.

where $\delta_{dpp}X$ is the relative variation of parameter X , pp means plain profile while d_{pp} means double parabolic profiles.

Table 4 lists the comparison results. Note the absolute values of h_{\min} and Q are rounded to four decimal places as their differences are too small, while other results are rounded to two decimal places (the same as below). As expected, the h_{\min} sharply increases and the $P_{aspm\max}$ reduces to zero, which confirms the validity of double parabolic profiles regarding reducing edge wear. However, as the double parabolic profiles lead to a less capacity area, the load carrying capacity is reduced. So greater P_{\max} is generated to balance the external load, and the hydrodynamic friction force also increases which causes a greater P_f . It is obvious that Q is increased as the double parabolic

profiles increases the film pressure gradient at bushing edge, so the comprehensive effects of greater P_f and Q lead to a tiny increase of T_e based on equation (11).

The main motivation of this study is to increase load carrying capacity and reduce friction loss of the journal bearing with double parabolic profiles by using surface textures. Here the groove textures with rectangular sections are adopted as they are relatively easy to manufacture. As mentioned in the literature [24], textures locating at the downstream of the film pressure filed have a positive effect on the lubrication performance, so here the groove textures are set in this region of the journal bearing with double parabolic profiles, corresponding to the red rectangle in Figure 6, from 200° to 350° in circumferential direction and $0.1B$ to $0.9B$ in axial direction. The detailed

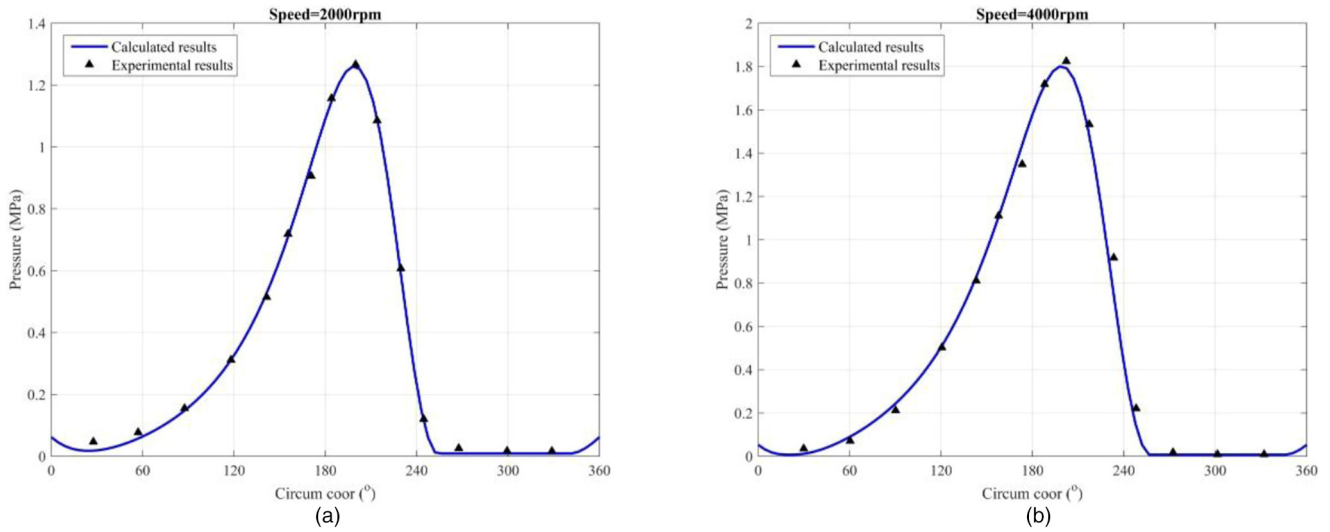


Fig. 5. Comparisons with Ferron's experimental results (a) Speed = 2000 rpm, (b) Speed = 4000 rpm.

Table 1. Detailed parameters of the journal bearing.

Parameters	Values
Lubricating oil	CD40
Oil feeding temperature ($^{\circ}\text{C}$)	70
Bearing diameter D (mm)	230
Bearing width B (mm)	90
Bearing bushing thickness d (mm)	5
Radial clearance c (mm)	0.14
Oil feeding groove ($^{\circ}$)	18
Standard deviations of the roughness of the bearing surface σ_b (μm)	0.8
Standard deviations of the roughness of the journal surface σ_j (μm)	0.4
Elastic modulus of copper-lead-tin alloy E_a (GPa)	97
Poisson's ratio of copper-lead-tin alloy ν_a	0.3
External moment M_e (Nm)	2000
Rotary speed (rpm)	1080

definitions of groove textures are illustrated in Figure 7, and the effects of various groove sizes on lubrication performance will be discussed in the subsequent analysis.

4.1 The effects of various groove depths

In this section, the effects of various groove depths are discussed. The parameter configurations for this section are listed in Table 5, and corresponding calculated results are listed in Table 6.

The relative variations of each performance parameter between plain profile and double parabolic profiles with groove textures is defined as below

$$\delta_{dppgt}X = \frac{X_{dppgt} - X_{pp}}{X_{pp}} \times 100\% \quad (27)$$

where $dppgt$ means double parabolic profiles with groove textures. In order to show the performance variations between double parabolic profiles and double parabolic profiles with groove textures more clearly, the $\delta_{dpp}X$ and $\delta_{dppgt}X$ are compared and listed in Table 7.

According to Tables 6 and 7, it is obviously that the groove textures positively affect the lubrication performance. Compared with the case of plain profile, the grooves with 20 μm depth give the best results regarding increasing load carrying capacity and reducing friction loss, as the P_{\max} only increases by 1.60% and the P_f has reduced by 3.19%. These variations can be explained that, the groove textures locating at the downstream of the film pressure filed can be seen as oil conservators, which extend the full film region and reduce the cavitation area, hence the hydrodynamic effect of the lubricating oil is strengthened and a recovery of the film pressure is generated, as illustrated in Fig. 8. The similar conclusions can also be found in the literature [8]. The pressure recovery effect is more evident with deeper groove depth, so the load carrying capacity increases more significantly.

Moreover, the hydrodynamic friction force arising from the shearing of oil reduces with the thicker oil film, which causes less friction loss. It can also be seen that, the grooves with shallower depth increase the leakage flowrate a little while for the grooves with 20 μm depth, the increase is even less than that of the double parabolic profiles. Based on equation (11), the comprehensive effects of the reduced friction loss and increased leakage flowrate lead to a tiny decrease of the effective temperature.

4.2 The effects of various groove lengths

In this section, the effects of various groove lengths are discussed. The parameter configurations for this section are listed in Table 8, and corresponding calculated results are listed in Table 9. Similarly, the $\delta_{dpp}X$ and $\delta_{dppgt}X$ are compared and listed in Table 10.

Table 2. Mesh schemes for mesh refinement analysis.

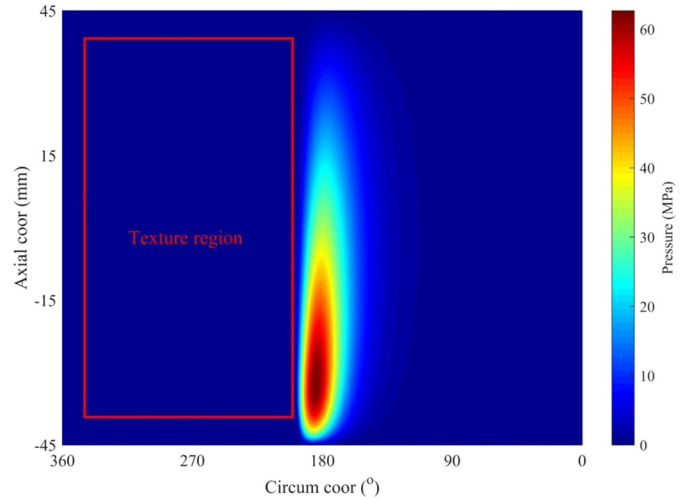
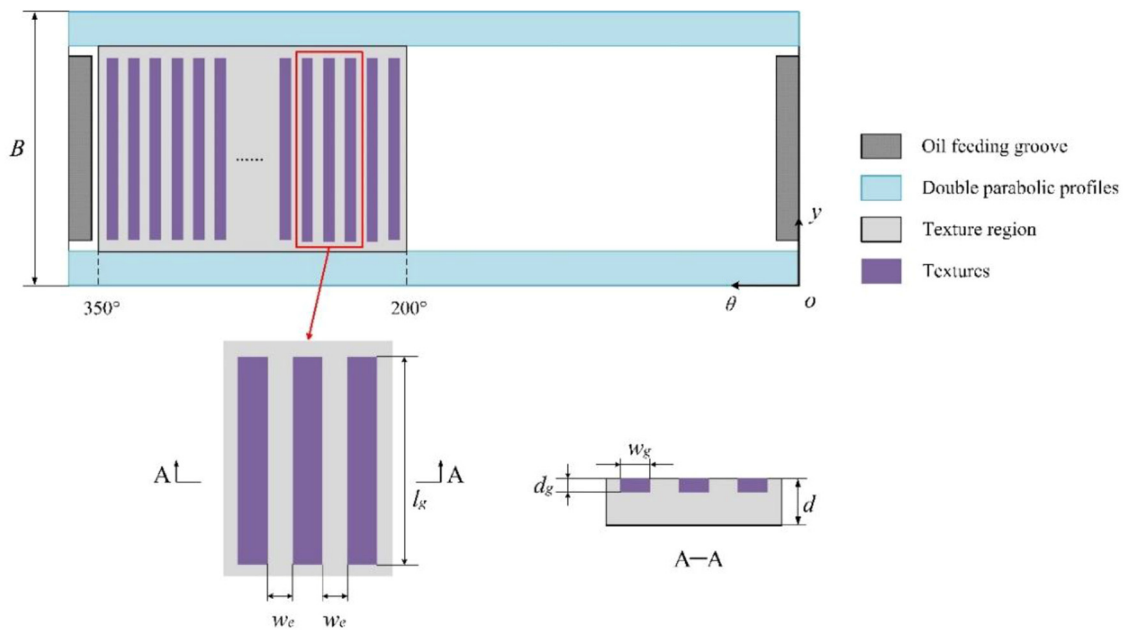
Scheme	1	2	3	4	5
$n_\theta \times n_\gamma$	721×121	1081×151	1441×181	1441×211	1801×211
h_{\min} (μm)	1.9417	1.9347	1.9095	1.9103	1.8974
Solving time (hour)	0.5064	1.4835	3.4378	3.8427	5.5708

Table 3. Parameters used to evaluate performance.

Parameters	Names	Units
Minimum film thickness	h_{\min}	μm
Maximum asperity contact pressure	P_{aspmax}	MPa
Maximum film pressure	P_{max}	MPa
Friction loss	P_f	W
Leakage flowrate	Q	$10^{-4} \text{ m}^3/\text{s}$
Effective temperature	T_e	$^\circ\text{C}$

Table 4. Performance comparisons between plain profile (pp) and double parabolic profiles (dpp).

X	pp	dpp	$\delta_{dpp}X$ (%)
h_{\min} (μm)	1.9095	3.2277	+69.03
P_{aspmax} (MPa)	0.66	0.00	-100.00
P_{max} (MPa)	60.03	62.67	+4.40
P_f (W)	4130.50	4178.78	+1.17
Q ($10^{-4} \text{ m}^3/\text{s}$)	1.2720	1.2818	+0.77
T_e ($^\circ\text{C}$)	86.68	86.75	+0.08

**Fig. 6.** Texture region of the journal bearing with double parabolic profiles.**Fig. 7.** Detailed definitions of the groove textures.

Tables 9 and 10 show that, compared with the case of plain profile, the P_{\max} reduces by 3.08% in the 40 mm case, while increases by 12.01% in the 60 mm case, which is much greater than that of double parabolic profiles. The reason for this phenomenon is that the pressure recovery effect, as explained previously, is more evident than other cases when the groove length is 60 mm, and the maximum recovery pressure is even greater than the maximum film pressure in untextured region, as illustrated in Figure 9.

Moreover, it can be seen that all the grooves textures reduce the friction loss in different extents, specifically, the longer groove length leads to thicker oil film, which causes less friction loss. It can also be seen the leakage

flowrate increases a little in all cases, while these increases show no obvious regularity. As mentioned before, the effective temperature shows a tiny decrease due to the comprehensive effects of the friction loss and leakage flowrate.

4.3 The effects of various groove densities

In this section, the effects of various groove densities are discussed. Note the total area of groove textures, $S_g = w_g \times l_g \times n_g$, are constant, while the w_g , w_e , and n_g are various among cases. Here the groove numbers n_g is used to represent the density, and greater n_g means denser grooves and vice versa. The parameter configurations for this section are listed in Table 11, and corresponding calculated results are listed in Table 12. Similarly, the $\delta_{dpp}X$ and $\delta_{dppgt}X$ are compared and listed in Table 13.

Tables 12 and 13 show that, compared with the case of plain profile, the case of 60 grooves has a superior performance than others on increasing load carrying capacity and reducing friction loss, while followed by the case of 20 grooves, which is contrary to our expectation. This phenomenon shows that there is no obvious linear relationship between the groove densities and lubrication performance, which may be more dependent on the specific operating conditions and geometric parameters of the journal bearing. For the bearing investigated in this study, the case of 60 grooves within given densities can meet our

Table 5. Parameter configurations for Section 4.1.

	Names	Values
Groove width (mm)	w_g	3
Groove gap (mm)	w_e	2
Groove length (mm)	l_g	50
Groove numbers	n_g	60
Mesh of single groove	$n_{g\theta} \times n_{gy}$ (circum \times axial)	6×100
Groove depths (μm)	d_g	5, 10, 15, 20

Table 6. Calculated results of double parabolic profiles with groove textures with various groove depths.

X	$d_g = 5 \mu\text{m}$	$d_g = 10 \mu\text{m}$	$d_g = 15 \mu\text{m}$	$d_g = 20 \mu\text{m}$
h_{\min} (μm)	3.2637	3.2878	3.3592	4.0175
$P_{aspm\max}$ (MPa)	0.00	0.00	0.00	0.00
P_{\max} (MPa)	62.52	62.36	62.15	60.99
P_f (W)	4130.28	4110.51	4113.68	3998.57
Q ($10^{-4}\text{m}^3/\text{s}$)	1.2840	1.2843	1.2922	1.2812
T_e ($^{\circ}\text{C}$)	86.51	86.43	86.34	86.02

Table 7. Comparisons between $\delta_{dpp}X$ and $\delta_{dppgt}X$ with various groove depths.

X	$\delta_{dpp}X$ (%)	$\delta_{dppgt}X$ (%) ($d_g = 5\mu\text{m}$)	$\delta_{dppgt}X$ (%) ($d_g = 10\mu\text{m}$)	$\delta_{dppgt}X$ (%) ($d_g = 15\mu\text{m}$)	$\delta_{dppgt}X$ (%) ($d_g = 20\mu\text{m}$)
h_{\min}	+69.03	+70.92	+72.18	+75.92	+110.40
$P_{aspm\max}$	-100.00	-100.00	-100.00	-100.00	-100.00
P_{\max}	+4.40	+4.15	+3.88	+3.53	+1.60
P_f	+1.17	-0.01	-0.48	-0.41	-3.19
Q	+0.77	+0.94	+0.97	+1.59	+0.72
T_e	+0.08	-0.20	-0.29	-0.39	-0.76

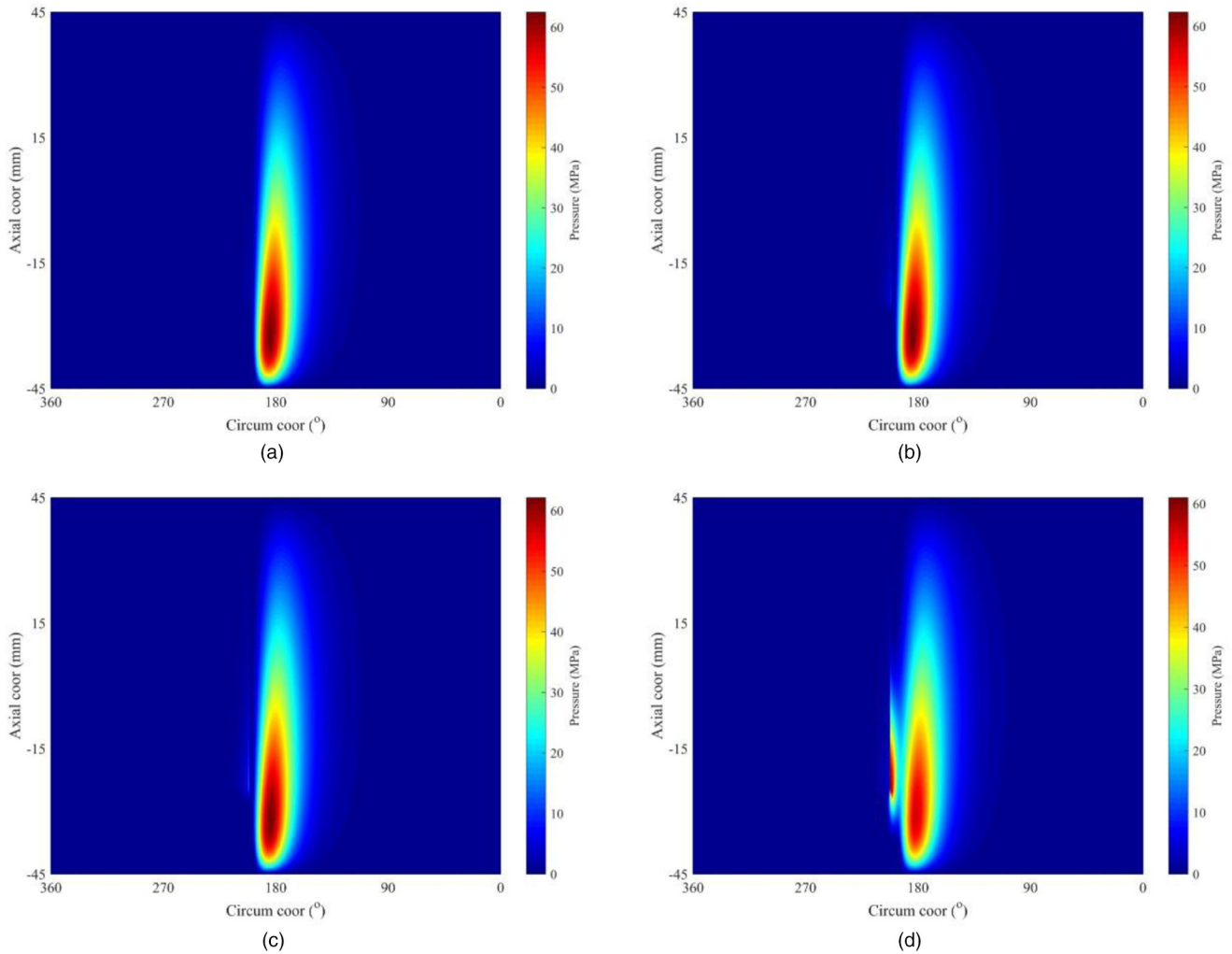


Fig. 8. Film pressures of double parabolic profiles with groove textures with various groove depths (a) $d_g = 5 \mu\text{m}$, (b) $d_g = 10 \mu\text{m}$, (c) $d_g = 15 \mu\text{m}$, (d) $d_g = 20 \mu\text{m}$.

Table 8. Parameter configurations for Section 4.2.

	Names	Values
Groove width (mm)	w_g	3
Groove gap (mm)	w_e	2
Groove depths (μm)	d_g	20
Groove numbers	n_g	60
Groove length (mm)	l_g	30, 40, 50, 60
Mesh of single groove	$n_{g\theta} \times n_{gy}$ (circum \times axial)	$6 \times 60, 6 \times 80,$ $6 \times 100, 6 \times 120$

purpose well. As expected, the variations of leakage flowrate and effective temperatures are all tiny which have been explained previously.

5 Conclusions

A numerical analysis is conducted to investigate the effects of double parabolic profiles with groove textures on the hydrodynamic performance of a specific journal bearing under steady operating conditions. The grooves are set in the downstream of the pressure field and the effects of various groove depths, lengths, and densities are discussed. Following conclusions can be drawn from the numerical results:

- Compared with the case of plain profile, the double parabolic profiles can sharply increase the minimum film thickness and reduce the asperity contact pressure to zero. However, the visible drawbacks of this profile are that it also reduces the load carrying capacity and increases friction loss.
- Compared with the case of plain profile, the double parabolic profiles with groove textures with given depths affect the lubrication performance positively due to the

Table 9. Calculated results of double parabolic profiles with groove textures with various groove lengths.

X	$l_g = 30$ mm	$l_g = 40$ mm	$l_g = 50$ mm	$l_g = 60$ mm
h_{\min} (μm)	3.4925	3.716	4.0175	4.2763
P_{aspmax} (MPa)	0.00	0.00	0.00	0.00
P_{max} (MPa)	60.97	58.18	60.99	67.24
P_f (W)	4114.87	4049.50	3998.57	3954.67
Q ($10^{-4}\text{m}^3/\text{s}$)	1.2931	1.2783	1.2812	1.2804
T_e ($^{\circ}\text{C}$)	86.34	86.26	86.02	85.87

Table 10. Comparisons between $\delta_{dpp}X$ and $\delta_{dppgt}X$ with various groove lengths.

X	$\delta_{dpp}X$ (%)	$\delta_{dppgt}X$ (%) ($l_g = 30$ mm)	$\delta_{dppgt}X$ (%) ($l_g = 40$ mm)	$\delta_{dppgt}X$ (%) ($l_g = 50$ mm)	$\delta_{dppgt}X$ (%) ($l_g = 60$ mm)
h_{\min}	+69.03	+82.90	+94.61	+110.40	+123.95
P_{aspmax}	-100.00	-100.00	-100.00	-100.00	-100.00
P_{max}	+4.40	+1.56	-3.08	+1.60	+12.01
P_f	+1.17	-0.38	-1.96	-3.19	-4.26
Q	+0.77	+1.66	+0.50	+0.72	+0.66
T_e	+0.08	-0.39	-0.48	-0.76	-0.93

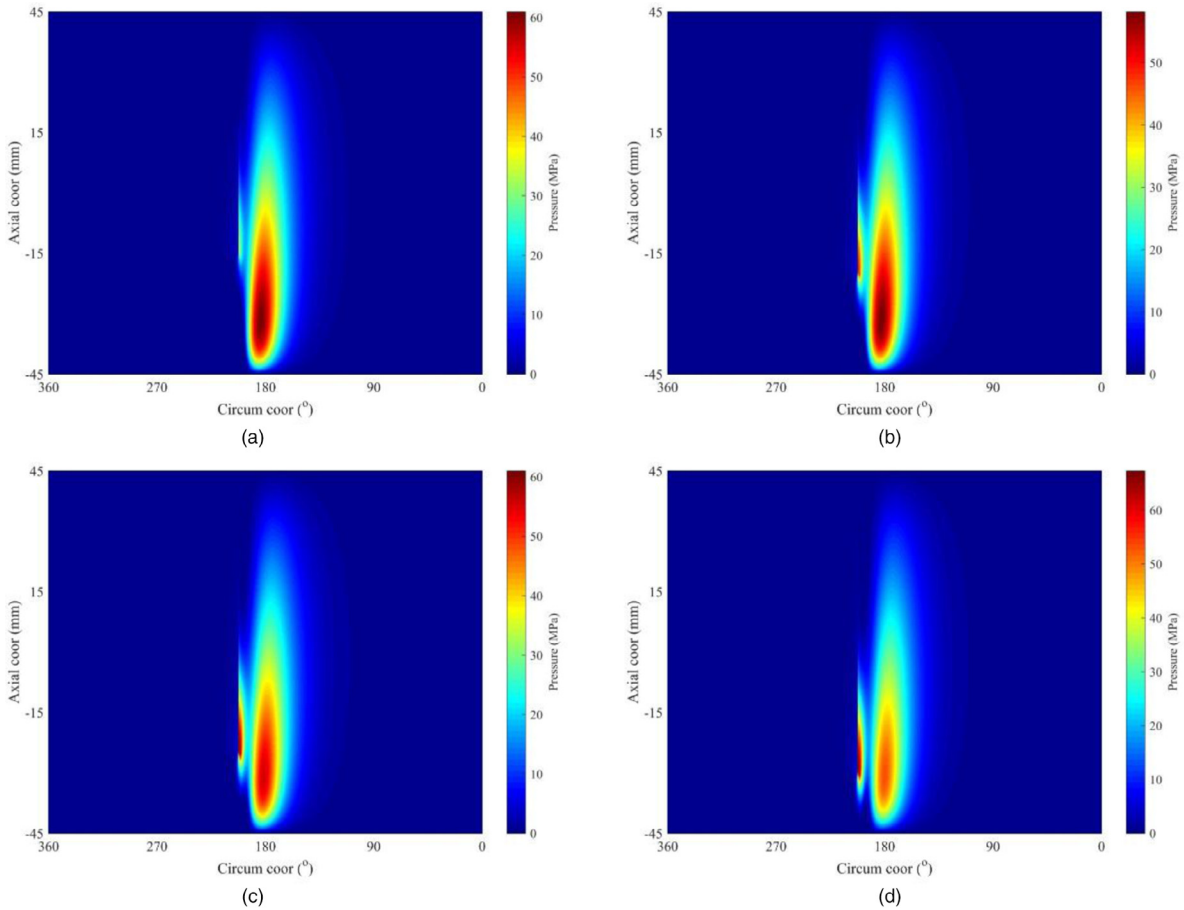


Fig. 9. Film pressures of double parabolic profiles with groove textures with various groove lengths (a) $l_g = 30$ mm, (b) $l_g = 40$ mm, (c) $l_g = 50$ mm, (d) $l_g = 60$ mm.

Table 11. Parameter configurations for Section 4.3.

	Names	Values
Groove width (mm)	w_g	3, 4.5, 9
Groove gap (mm)	w_e	2, 3, 6
Groove numbers	n_g	60, 40, 20
Groove length (mm)	l_g	50
Groove depths (μm)	d_g	20
Mesh of single groove	$n_{g\theta} \times n_{gy}$ (circum \times axial)	6×100 , 9×100 , 18×100

Table 12. Calculated results of double parabolic profiles with groove textures with various groove densities.

X	$n_g = 60$	$n_g = 40$	$n_g = 20$
h_{\min} (μm)	4.0175	3.2984	3.3414
$P_{asppmax}$ (MPa)	0.00	0.00	0.00
P_{max} (MPa)	60.99	61.90	61.61
P_f (W)	3998.57	4116.86	4098.00
Q ($10^{-4}\text{m}^3/\text{s}$)	1.2812	1.2763	1.2779
T_e ($^{\circ}\text{C}$)	86.02	86.56	86.46

Table 13. Comparisons between $\delta_{dpp}X$ and $\delta_{dppgt}X$ with various groove densities.

X	$\delta_{dpp}X$ (%)	$\delta_{dppgt}X$ (%) ($n_g = 60$)	$\delta_{dppgt}X$ (%) ($n_g = 40$)	$\delta_{dppgt}X$ (%) ($n_g = 20$)
h_{\min}	+69.03	+110.40	+72.74	+74.99
$P_{asppmax}$	-100.00	-100.00	-100.00	-100.00
P_{max}	+4.40	+1.60	+3.11	+2.63
P_f	+1.17	-3.19	-0.33	-0.79
Q	+0.77	+0.72	+0.34	+0.46
T_e	+0.08	-0.76	-0.14	-0.25

pressure recovery effect in textured region. This effect is more evident with deeper groove depth, which increases the load carrying capacity more significantly. Meanwhile, the thicker oil film reduces the friction force arising from the shearing of lubricating oil, which causes less friction loss.

- In the case of longer groove length, the maximum recovery pressure in textured region may even be greater than the maximum film pressure in untextured region due to the pressure recovery effect.
- The groove textures with various densities improve the lubrication performance in different extents. However, there is no obvious linear relationship between the groove densities and performance enhancement, which may be due to the specific operating conditions and geometric parameters.

- Compared with the case of plain profile, the variations of leakage flowrate and effective temperatures are all tiny, which shows that setting increasing load carrying capacity and reducing friction loss as the main optimization purposes is reasonable.
- For the journal bearing investigated in this paper, the double parabolic profiles with groove textures with $w_g = 3$ mm, $w_e = 2$ mm and $l_g = 50$ mm, which are located in the region from 200° to 350° in circumferential direction and $0.1B$ to $0.9B$ in axial direction can meet our purpose well.

The cavitation area of oil film determined by Reynolds boundary conditions may be less accurate than mass-conservative treatment, which is a limitation of this study. In future work, cavitation effects will be treated in mass-conserving way, and some optimization methods will be adopted to determine the optimal texture design.

Nomenclature

D	Bearing diameter
B	Width of plain profile
d	Thickness of plain profile
L_y	Axial width of double parabolic profiles
L_z	Radial height of double parabolic profiles
h	Film thickness
h_g	Film thickness without elastic deformation
c	Radial clearance
e	Eccentricity of the midplane
φ	Attitude angle of the midplane
γ	Misalignment angle
δ_z	Variation clearance caused by double parabolic profiles
δ_{tex}	Variation clearance caused by groove textures
δ_e	Elastic deformation of bushing surface
E	Elastic modulus of the bushing
ν	Poisson's ratio of the bushing
μ	Viscosity of lubricating oil
p	Film pressure
U_1, U_2	Velocities of the two surfaces
σ	Standard deviation of combined roughness
ϕ_x, ϕ_y	Pressure flow factors
ϕ_s	Shear flow factor
h_T	Local film thickness
ω	Angular velocity of journal
P_{asp}	Asperity contact pressure
η	The number of asperities per unit area
β	The mean radius of curvature of the asperities
E	Composite elastic modulus
$F_{2.5}(h/\sigma)$	Gaussian distribution function
$\phi_f, \phi_{fs}, \phi_{fp}$	Shear stress factors
μ_{asp}	Boundary friction coefficient
f	Friction force
P_f	Friction loss
Q_1	Leakage flowrate from the front end plane
Q_2	Leakage flowrate from the rear end plane
Q	Total leakage flowrate
T_e	Effective temperature of lubricating oil

T_i	Inlet oil temperature
ρ	Density of lubricating oil
c_l	Specific heat of lubricating oil
M_e	External moment
M_t	Resultant moment
M_{oil}	Hydrodynamic moment
M_{asp}	Asperity contact moment
M_{ex}, M_{ez}	External applied moment along the x and z axes
M_{tx}, M_{tz}	Resultant moment along the x and z axes
M_{oilx}, M_{oilz}	Hydrodynamic moment along the x and z axes
M_{aspz}, M_{aspx}	Asperity contact moment along the x and z axes
ω_s	Overrelaxation factor
ε_p	Allowable precision for the solution of film pressure
ε_t	Allowable precision for the solution of the effective temperature
ε	Eccentricity ratio of the midplane
M_e	Amplitude of external moment
M_t	Amplitude of resultant moment
ω_φ	Correction factor of φ
ω_ε	Correction factor of ε
ω_γ	Correction factor of γ
err_{xz}, err_M	Allowable precision for the calculation of load equilibrium
σ_b	Standard deviations of the roughness of the bearing surface
σ_j	Standard deviations of the roughness of the journal surface
n_θ, n_y	Numbers of nodes along the circumferential and axial direction
h_{min}	Minimum film thickness
P_{max}	Maximum film pressure
$P_{asp\ max}$	Maximum asperity contact pressure
w_g	Groove width
w_e	Groove gap
l_g	Groove length
n_g	Groove numbers
$n_{g\theta} \times n_{gy}$	Mesh of single groove
d_g	Groove depth
S_g	Total area of groove textures

This work is supported by the Fundamental Research Funds for the Central Universities (3072019CFM0302) and National Natural Science Foundation of China (51809057).

References

- [1] P.S. Leung, I.A. Craighead, T.S. Wilkinson, An analysis of the steady state and dynamic characteristics of a spherical hydrodynamic journal bearing, *J. Tribol.* **111**, 459–467 (1989)
- [2] H.A. El-Gamal, Analysis of the steady state performance of a wedge-shaped hydrodynamic journal bearing, *Wear* **184**, 111–117 (1995)
- [3] H.E. Rasheed, The elastohydrodynamic lubrication of heavily loaded journal bearing having non-cylindrical axial geometry, *Tribol. Ser.* **32**, 675–683 (1997)
- [4] S. Strzelecki, Operating characteristics of heavy loaded cylindrical journal bearing with variable axial profile, *Mater. Res.* **8**, 481–486 (2005)
- [5] A. Mihailidis, V. Bakolas, K. Panagiotidis, K. Poullos, C. Sachanas, Influence of the bushing geometry on the thermohydrodynamic performance of a misaligned journal bearing, *Proc. Inst. Mech. Eng. J* **224**, 37–53 (2010)
- [6] C. Liu, B. Zhao, W. Li, X. Lu, Effects of bushing profiles on the elastohydrodynamic lubrication performance of the journal bearing under steady operating conditions, *Mech. Ind.* **20**, 207 (2019)
- [7] J.-H. Ji, C.-W. Guan, Y.-H. Fu, Effect of micro-dimples on hydrodynamic lubrication of textured sinusoidal roughness surfaces, *Chin. J. Mech. Eng.* **31** (2018)
- [8] B. Manser, I. Belaidi, A. Hamrani, S. Khelladi, F. Bakir, Performance of hydrodynamic journal bearing under the combined influence of textured surface and journal misalignment: a numerical survey, *Compt. Rend. Mécan.* **347**, 141–165 (2019)
- [9] A.B. Shinde, P.M. Pawar, Effect of partial grooving on the performance of hydrodynamic journal bearing, *Ind. Lubric. Tribol.* **69**, 574–584 (2017)
- [10] H. Zhang, M. Hafezi, G. Dong, Y. Liu, A design of coverage area for textured surface of sliding journal bearing based on genetic algorithm, *J. Tribol.* **140** (2018) <https://doi.org/10.1115/1.4039958>
- [11] H. Zhang, Y. Liu, M. Hua, D. Zhang, L. Qin, G. Dong, An optimization research on the coverage of micro-textures arranged on bearing sliders, *Tribol. Int.* **128**, 231–239 (2018)
- [12] F.M. Meng, W. Zhang, Effects of compound groove texture on noise of journal bearing, *J. Tribol.* **140** (2018) <https://doi.org/10.1115/1.4038353>
- [13] F. Meng, H. Yu, C. Gui, L. Chen, Experimental study of compound texture effect on acoustic performance for lubricated textured surfaces, *Tribol. Int.* **133**, 47–54 (2019)
- [14] H. Yamada, H. Taura, S. Kaneko, Numerical and experimental analyses of the dynamic characteristics of journal bearings with square dimples, *J. Tribol.* **140** (2018) <https://doi.org/10.1115/1.4037151>
- [15] H. Yamada, H. Taura, S. Kaneko, Static Characteristics of journal bearings with square dimples, *J. Tribol.* **139** (2017) <https://doi.org/10.1115/1.4035778>
- [16] C. Gu, X. Meng, D. Zhang, Y. Xie, Transient analysis of the textured journal bearing operating with the piezoviscous and shear-thinning fluids, *J. Tribol.* **139** (2017) <https://doi.org/10.1115/1.4035812>
- [17] N.J. Morris, H. Shahmohamadi, R. Rahmani, H. Rahnejat, C.P. Garner, Combined experimental and multiphase computational fluid dynamics analysis of surface textured journal bearings in mixed regime of lubrication, *Lubric. Sci.* **30**, 161–173 (2018)
- [18] H. Zhang, G. Dong, M. Hua, F. Guo, K.S. Chin, Parametric design of surface textures on journal bearing, *Ind. Lubric. Tribol.* **67**, 359–369 (2015)
- [19] L. Wang, Z. Han, G. Chen, H. Su, Thermo-hydrodynamic analysis of large-eccentricity hydrodynamic bearings with texture on journal surface, *Proc. Inst. Mech. Eng. Part C* **232**, 3564–3569 (2017)
- [20] S. Matele, K.N. Pandey, Effect of surface texturing on the dynamic characteristics of hydrodynamic journal bearing comprising concepts of green tribology, *Proc. Inst. Mech. Eng. Part J* **232**, 1365–1376 (2018)

- [21] R. Yu, W. Chen, P. Li, The analysis of elastohydrodynamic lubrication in the textured journal bearing, *Proc. Inst. Mech. Eng., Part J* **230**, 1197–1208 (2016)
- [22] Q. Lin, Q. Bao, K. Li, M.M. Khonsari, H. Zhao, An investigation into the transient behavior of journal bearing with surface texture based on fluid-structure interaction approach, *Tribol. Int.* **118**, 246–255 (2018)
- [23] A.B. Shinde, P.M. Pawar, Multi-objective optimization of surface textured journal bearing by Taguchi based Grey relational analysis, *Tribol. Int.* **114**, 349–357 (2017)
- [24] N. Tala-Ighil, M. Fillon, P. Maspeyrot, Effect of textured area on the performances of a hydrodynamic journal bearing, *Tribol. Int.* **44**, 211–219 (2011)
- [25] N. Tala-Ighil, M. Fillon, A numerical investigation of both thermal and texturing surface effects on the journal bearings static characteristics, *Tribol. Int.* **90**, 228–239 (2015)
- [26] M. Rades, Dynamic analysis of an inertial foundation model, *Int. J. Solids Struct.* **8**, 1353–1372 (1972)
- [27] J. Sun, C.L. Gui, Z.H. Wang, Research on elastohydrodynamic lubrication of a crankshaft bearing with a rough surface considering crankshaft deformation, *Proc. Inst. Mech. Eng. Part D* **222**, 2403–2414 (2008)
- [28] C.R. Lin, J. H. G. Rylander, Performance characteristics of compliant journal bearings, *J. Tribol.* **113**, 639–644 (1991)
- [29] S.B. Glavatskih, M. Fillon, TEHD analysis of thrust bearings with ptfе-faced pads, *Proceedings of 2004 ASME/STLE International Joint Tribology Conference* (2004) <https://doi.org/10.1115/TRIB2004-64178>
- [30] K. Thomsen, P. Klit, A study on compliant layers and its influence on dynamic response of a hydrodynamic journal bearing, *Tribol. Int.* **44**, 1872–1877 (2011)
- [31] N. Patir, H.S. Cheng, An average flow model for determining effects of threedimensional roughness on partial hydrodynamic lubrication, *J. Lubric. Technol.* **100**, 12–17 (1978)
- [32] N. Patir, M.S. Cheng, Application of average flow model to lubrication between rough sliding surfaces, *J. Lubric. Technol.* **101**, 220–229 (1979)
- [33] J.A. Greenwood, J.H. Tripp, The contact of two nominally flat rough surfaces, *Proc. Inst. Mech. Eng.* **185**, 625–633 (2016)
- [34] F. Lv, Z. Rao, N. Ta, C. Jiao, Mixed-lubrication analysis of thin polymer film overlaid metallic marine stern bearing considering wall slip and journal misalignment, *Tribol. Int.* **109**, 390–397 (2017)
- [35] S. Wen, P. Huang, *Principles of Tribology* (Fourth Edition), Tsinghua University Press, Beijing (2012)
- [36] J. Ferron, J. Frene, R. Boncompain, A study of the thermohydrodynamic performance of a plain journal bearing comparison between theory and experiments, *J. Lubric. Technol.* **105**, 422–428 (1983)
- [37] D. Gropper, L. Wang, T.J. Harvey, Hydrodynamic lubrication of textured surfaces: A review of modeling techniques and key findings, *Tribol. Int.* **94**, 509–529 (2016)

Cite this article as: C. Liu, W. Li, X. Lu, B. Zhao, Effects of double parabolic profiles with groove textures on the hydrodynamic lubrication performance of journal bearing under steady operating conditions, *Mechanics & Industry* **21**, 301 (2020)